Catalysis Today 156 (2010) 173–180

Contents lists available at ScienceDirect

Catalysis Today

journal homepage: www.elsevier.com/locate/cattod

Design of asymmetric multilayer membranes based on mixed ionic–electronic conducting composites supported on Ni–Al foam substrate

V. Sadykov[a,b,*], V. Zarubina[a,b], S. Pavlova[a], T. Krieger[a], G. Alikina[a], A. Lukashevich[a], V. Muzykantov[a], E. Sadovskaya[a], N. Mezentseva[a], E. Zevak[a,b], V. Belyaev[a], O. Smorygo[c]

[a] Boreskov Institute of Catalysis SB RAS, pr. Lavrentieva, 5, Novosibirsk 630090, Russia
[b] Novosibirsk State University, Novosibirsk, Russia
[c] Powder Metallurgy Institute, Minsk, Belarus

ARTICLE INFO

Article history:
Available online 18 September 2010

Keywords:
Oxygen-conducting supported membranes
Oxygen separation
Mixed ionic–electronic conducting nanocomposites
Perovskites
Fluorites
Alloy foam substrate
CH_4
Syngas

ABSTRACT

This paper presents the results of research aimed at design of multilayer asymmetric oxygen separation membranes comprised of functionally graded by composition and porosity nanocomposite layers with mixed ionic–electronic conductivity (MIEC) and a high oxygen mobility supported on the compressed Ni–Al alloy foam substrate. Complex oxides with fluorite-like structure ($Ce_{0.9}Gd_{0.1}O_{2-\delta}$), perovskite-like structure $La_{0.8}Sr_{0.2}Fe_{1-x}Ni_xO_{3-\delta}$ ($x = 0.3$–0.4) and spinel structure $MnFe_2O_4$ synthesized via polymerized precursors (Pechini) route were used for the preparation of these nanocomposites by ultrasonic dispersion of their mixtures in isopropanol with addition of polyvinyl butyral. Parameters characterizing their oxygen mobility and reactivity were estimated by oxygen isotope heteroexchange, weight loss transients, temperature-programmed reduction by CH_4 and reoxidation by CO_2. Membranes were prepared by successively supporting on one side of substrate macroporous–mesoporous–microporous-dense layers of MIEC nanocomposites finally covered by a porous layer of La–Ni–Pt/$Pr_{0.3}Ce_{0.35}Zr_{0.35}O_{2-x}$ catalyst. Preliminary tests of this membrane in the lab-scale reactor in the process of methane selective oxidation/oxi-dry reforming into syngas demonstrated their oxygen permeability and performance promising for the practical application.

1. Introduction

Mixed ionic–electronic conducting (MIEC) oxide composites comprised of electronic conductors and ionic conductors are the most promising membrane materials due to combination of mechanical and chemical stability with a high oxygen permeability provided by interfaces as paths for fast oxygen diffusion [1–6]. Dense oxygen permselective MIEC ceramic membranes have a great potential for catalytic high-temperature processes including methane reforming into syngas [7–12]. However, for thick membranes, the bulk diffusion limits the oxygen permeability [4–6]. For thin membranes, kinetics of the surface processes on both membranes sides becomes the rate-limiting. In this case, supporting a porous oxide layer with a high rate of O_2 activation on a dense non-porous MIEC layer membrane or using a microporous MIEC substrate is known to increase the oxygen flux [4–6,13–16]. A number of studies clearly showed the promising features of asymmetric supported membranes for high-performance oxygen separation [2,4–7,15,16]. However, the fabrication of such membranes is still a challenge because of difficulty in obtaining porous supports with desirable properties in terms of pore size, gas permeability, thermal/mechanical stability and compatibility with MIEC materials by thermal expansion coefficients (TEC).

One of the promising approaches is based upon consecutive deposition of MIEC nanocomposite layers with graded porosity and chemical composition on a robust macroporous substrate [15]. Ni–Al alloy compressed foam of a high thermal stability and mechanical strength due to segregated corundum surface layer [17] earlier used successfully as support for nanocomposite catalysts of internal CH_4 steam reforming in solid oxide fuel cells (SOFC) [17,18] seems to be promising for design of supported asymmetric membranes as well. MIEC nanocomposites comprised of $Ce_{0.9}Gd_{0.1}O_{2-\delta}$ (GDC) fluorite and $La_{0.8}Sr_{0.2}Fe_{1-x}Ni_xO_{3-\delta}$ ($x = 0.3$–0.4) (LSFN$_x$) perovskite earlier shown to be promising for design of functionally graded SOFC cathodes [20–22] due to their high lattice oxygen mobility and activity in dissociation of oxygen molecules appear to be attractive for design of supported membranes as well. Moreover, these nanocomposites are compatible both with Ni–Al alloy substrate and such certified protective layers from the fuel side as

* Corresponding author at: Boreskov Institute of Catalysis SB RAS, pr. Lavrentieva, 5, Novosibirsk 630090, Russia.
E-mail addresses: sadykov@catalysis.ru, vasadykov@mail.ru (V. Sadykov).

0920-5861/$ – see front matter © 2010 Elsevier B.V. All rights reserved.
doi:10.1016/j.cattod.2010.07.030

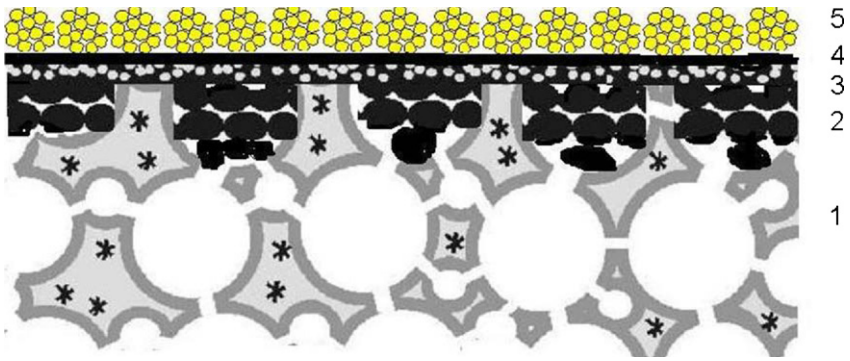

Fig. 1. A scheme of asymmetric supported membrane. 1 – Ni–Al compressed foam substrate, 2 – macroporous nanocomposite layer, 3 – mesoporous/microporous nanocomposite layer, 4 – dense nanocomposite layer, 5 – porous catalytic layer. * – segregated corundum needles.

Sm-doped ceria (SDC) [23] or its composite with $MnFe_2O_4$ (MF) [12], the latter required to prevent reductive decomposition of perovskites leading to catastrophic mechanical failure of membranes [24]. Both GDC–MF and GDC–$LSFN_{0.3}$ composites have the TEC value $\sim 12 \times 10^{-6}$ which is close to that of Ni–Al foam substrate with segregated corundum layer. So these composites are indeed promising materials for supporting as MIEC layers on Ni–Al compressed foam.

For porous catalytic layer supported on the fuel side of membrane required to ensure a high performance in CH_4 transformation into syngas by the lattice oxygen, nanocomposite active component comprised of $LaNi_{0.9}Pt_{0.1}O_3$/$Pr_{0.3}Ce_{0.35}Zr_{0.35}O_{2-x}$ shown to be highly active and stable to coking in CH_4 steam reforming in feeds with a small excess of steam [18,19] was selected.

This paper presents the results of research aimed at design of asymmetric multilayer membrane on Ni–Al foam substrate and its lab-scale testing in the process of methane selective oxidation/oxidry reforming into syngas. The main purpose of this work was to elaborate procedures for successive layers supporting, to check compatibility of selected MIEC materials, to estimate the oxygen permeability and performance characteristics and to verify their stability in realistic operation conditions.

2. Experimental

2.1. Composite synthesis and characterization

Starting complex oxides were prepared by modified Pechini route as described in details elsewhere [18–22]. Nanocomposites were synthesized via ultrasonic dispersion of the mixture of $LSFN_x$ (or MF) and GDC powders in isopropanol in 1:1 weight ratio using a T25 ULTRA-TURRAX (IKA, Germany) homogenizer with addition of polyvinyl butyral (PVB) followed by drying, pressing pellets and their sintering in air (for LSFN + GDC composite) or in the Ar flow (for MF + GDC composite) up to 1370 °C [20–22]. For characterization of the structural features and oxygen mobility and reactivity, pellets were crushed and ball milled into powders.

XRD patterns were obtained with an ARLX'TRA diffractometer (Thermo, Switzerland) using Cu K_α monochromatic radiation ($\lambda = 1.5418$ Å) in 2θ range 5–90°.

The rate of the surface reaction of oxygen molecules activation and oxygen mobility of LSFN + GDC composite was characterized by the oxygen isotope heteroexchange. These experiments were carried out both in static [20–22] and in flow installation (SSITKA mode [25]) with MS control of the gas phase isotope composition.

For dense LSFN perovskite and LSFN + GDC nanocomposite pellets, the oxygen chemical diffusion coefficients were estimated by analysis of their weight relaxation after step-wise change of O_2 content in the N_2 stream from 14% to 1.4% using a STA 409 PC "LUXX" NETZSCH machine.

The oxygen mobility and reactivity of MF + GDC nanocomposites designed for operation in reducing conditions at the fuel side of membrane were estimated by temperature-programmed reduction with 1% CH_4 in He and subsequent temperature-programmed reoxidation with 1% H_2O in He in the flow kinetic installation equipped with on-line PEM-2 M IR absorbance gas analyzer and electrochemical H_2 sensor following earlier described procedures [20–22]

2.2. Preparation of membrane

Macroporous open-cell nickel foam substrate was manufactured by the nickel electroplating of the polyurethane foam samples (cell density 60 ppi) followed by sintering in the dissociated ammonia atmosphere at 1100 °C for 1 h. The foam samples were then deformed by a uniaxial compression to 1 mm thickness modifying the cell morphology and decreasing porosity from 95.5% to 60–80%. Deformed foams were subjected to the pack aluminizing and then annealed at 1000 °C for 1 h under air to form a thin α-alumina layer over the foam cell walls/ribs for a better adhesion of composite layers.

Fabrication of a supported multilayer membrane followed the next steps. First, a disc cut from membrane was pressed and spark-welded into the stainless steel ring to prevent its bending under subsequent manipulation procedures. Then the cells of a foam support from one side of a membrane (Fig. 1) were filled with macroporous layer of a coarse (fraction up to 10 μm) particles of LSFN + GDC composite presintered at 1200 °C and ball milled. A thick viscous slurry of these particles in isopropanol with addition of PVB was supported on the substrate via slip casting. This procedure was repeated several times with intermediate drying and calcination at 900–1000 °C after each supporting until required uniform filling of foam cells for depth ~0.1 mm (Fig. 1, layer 2) was achieved. This layer provides nearly free air access and also serves as more or less plain and robust support for subsequent MIEC layers. For filling macropores between the coarse particles of composite and forming a mesoporous/microporous layer 3 (Fig. 1) with thickness 10–20 μm, a highly dispersed LSFN + GDC composite precalcined at 700 °C was next supported several times from suspension in isopropanol with addition of PVB. The function of this layer with developed gas–solid interface is activation of O_2 molecules and transfer of oxygen atoms to the dense MIEC layer, while providing pores for diffusion exchange of N_2 and O_2 molecules with the air stream. The gas-tight layer 4 (Fig. 1) (thickness ~10 μm) comprised of GDC + MF nanocomposite interpenetrating in part into the porous LSNF + GDC nanocomposite was supported on the layer 3 via slip casting of a slurry in isopropanol with addition of PVB. A special smoothing procedure was applied to restrict the thickness of this layer, thus keeping its upper sur-

Table 1
Some characteristics of samples sintered at 1200 °C.

Sample	SSA[a] (m^2/g)	Fluorite		Perovskite			
		Crystallite size (nm)	Lattice parameter (Å)	Crystallite size (nm)	Lattice parameters (Å)		
			a		*a*	*b*	*c*
$LSFNi_{0.3}$ + GDC	2.4	40	5.445	50	5.491	5.535	7.802

[a] Specific surface area for powders.

face at the level only slightly (<0.1 μm) higher than that of the foam cell ribs. To attain complete densification of this layer by sintering at 1200 °C under Ar flow, such additives as Cu, Bi and Ag nitrates were used. The function of this layer is to block nitrogen transfer through the membrane thus providing required selectivity of oxygen permeation. The gas-tight layer was washcoated by a porous catalytic layer 5 (Fig. 1) with thickness ~0.1 mm comprised of $Pr_{0.3}Ce_{0.35}Zr_{0.35}O_{2-x}$ complex oxide with La–Ni–Pt active component (~10 wt.% of $LaNi_{0.9}Pt_{0.1}O_3$) supported by the incipient wetness impregnation with the mixed solution of H_2PtCl_6 and La and Ni nitrates followed by calcination at 1000 °C. The function of this layer possessing reasonably high lattice oxygen mobility in $Pr_{0.3}Ce_{0.35}Zr_{0.35}O_{2-x}$ complex oxide [26] is to provide developed three-phase boundary from the fuel side of membrane required for the efficient transfer of oxygen atoms from the dense MIEC layer and their interaction with activated CH_4 molecules on the surface of catalyst particles. Finally, the main bulk of foam substrate and the surface of macropores in the coarse nanocomposite layer were covered with a thin (~50 nm) porous layer of $LSFN_{0.4}$ perovskite by membrane impregnation from the air side by a diluted suspension of nanosized particles in isopropanol with addition of PVB followed by drying and calcination at 1000 °C. This procedure aimed at increasing the oxygen flux through the membrane by facilitating spillover of surface oxygen species through substrate in reaction conditions.

2.3. Membrane reactor testing

To ensure the gas-tight sealing of supported disc membrane in titanium lab-scale reactor, it was first placed in specially designed copper washers, pre-sealed using Ag paste, pressed and preheated under Ar flow at 900 °C to provide a hermetic junction between the membrane steel ring and a copper washer/ring. Such a disc was inserted between two halves of specially designed Ti reactor, and the copper ring was compressed by using bolts and nuts ensuring required sealing.

The testing results were obtained for membrane with the working surface area of 1.1 cm^2. At the fuel stream outlet, a layer (about 1 cm^3) of the catalyst with the same active component $LaNi_{0.9}Pt_{0.1}O_3/Pr_{0.3}Ce_{0.35}Zr_{0.35}O_{2-x}$ supported on the microspherical γ-alumina was fixed between two Fechraloy gauzes protected by corundum layer supported by dust blasting technique [27].

The membrane reactor was tested in the flow kinetic installations using the feed of 4.5–20 vol.% CH_4 in He or 20 vol.% + 20 vol.% CO_2 in Ar (feed rate 1–15 L/h) and purified air (feed rate 0.7–45 L/h) supplied into the fuel and air parts of the reactor, respectively. Concentrations of reagents and products were determined by using gas chromatographic analysis and on-line IR absorbance gas analyzer PEM-2 M equipped with an electrochemical H_2 sensor [19].

Conversion of CH_4 (XCH_4, %) and selectivities of products (SCO and SH_2, %) were calculated using concentrations of components in the exit stream (denoted by square brackets []) as follows:

$$XCH_4 = 100\frac{[CO]+[CO_2]}{[CO]+[CO_2]+[CH_4]}$$

$$SCO = 100\frac{[CO]}{[CO]+[CO_2]}$$

$$SH_2 = 100\frac{[H_2]}{[H_2]+[H_2O]}$$

No carbon imbalance was observed within the limits of concentration analysis uncertainty (±5%).

The oxygen flux through the membrane under reaction conditions was estimated using results of analysis of the effluent composition and the flow rate value. Concentration of the oxygen-containing products in the effluent was either determined directly (CO and CO_2) or estimated using values of CH_4 conversion and H_2 selectivity (in the case of H_2O). The oxygen flux through the membrane is equal to the total flux of oxygen atoms at the reactor exit divided by 2 and related to the membrane surface area.

3. Results and discussion

3.1. Nanocomposites characterization

3.1.1. Structural features of composites

According to XRD data, $LSFN_x$–GDC composites are mainly comprised of perovskite and fluorite phases [20–22]. The sizes of perovskite and fluorite domains remain in the nanorange even in dense sample sintered at 1200 °C (Table 1).

For MF–GDC composite, along with reflections corresponding to fluorite and spinel phase, a new peak at $2\theta \sim 41°$ appears (Fig. 2). Its position corresponds to the perovskite-like phases such as complex ferrites-cobaltites [28], manganites [29] and nickelates [20–22]. Hence, some admixture of gadolinium ferrite-manganite perovskite-like phase could be formed in this system due to interac-

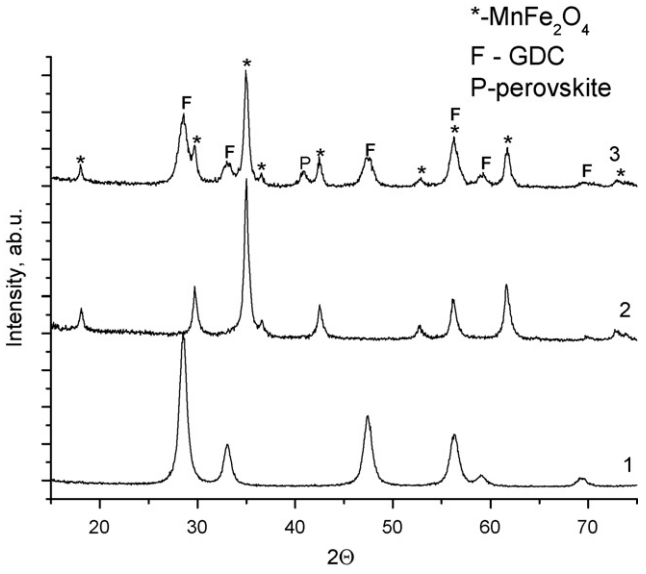

Fig. 2. XRD patterns of GDC (1), $MnFe_2O_4$ (2) and composite $MnFe_2O_4$ + GDC prepared by Pechini method (3).

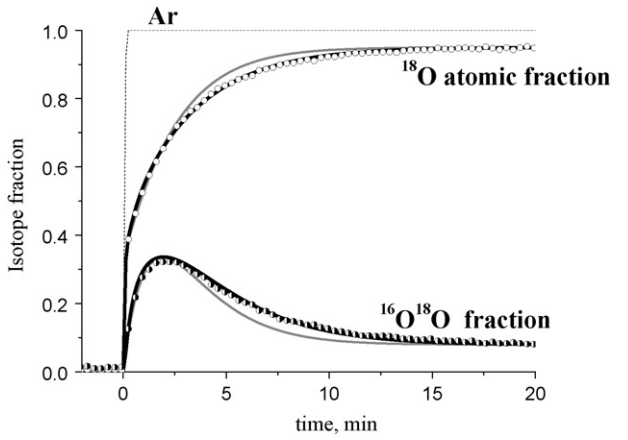

Fig. 3. Variation of ^{18}O and ^{16}O^{18}O fractions in the gas phase after switching the stream of 1% $^{16}O_2$ in He for the stream of 1% $^{18}O_2$ + 1% Ar in He at 700 °C. Points – experiment, gray line – fitting by the uniform diffusion model, black line – fitting by the heterogeneous diffusion model (Fig. 4).

tion between spinel and fluorite phases. This implies possibility of interaction between phases of MF–GDC and $LSFN_x$–GDC nanocomposites in the dense MIEC layer 4 (Fig. 1) affecting its oxygen permeation which requires further studies.

3.1.2. Mobility and reactivity of oxygen in nanocomposites

Oxygen isotope exchange. For powdered samples of LSFN–GDC nanocomposite sintered at high (1200 °C) temperatures, in the temperature-programmed mode of exchange in the static installation, a large amount of the lattice oxygen (up to 300–400 monolayers) was exchanged at temperatures ~700 °C, thus revealing a high bulk oxygen mobility in this temperature range [20–22].

More detailed information was obtained from results of SSITKA experiments (Fig. 3). Their detailed analysis with a due regard for the mechanism of oxygen isotope exchange, surface reaction and bulk diffusion was carried out by the inverse problem solution for the system of hyperbolic differential equations describing the isotope exchange in the flow reactor following earlier published approaches [25]. In the intermediate temperature range, all ^{16}O in the sample was exchanged for ^{18}O at typical times <1 h (Fig. 3), thus demonstrating a high bulk oxygen mobility. In contrary to earlier studied systems based upon doped ceria–zirconia solid solutions [25,26], for GDC–$LSFN_{0.3}$ nanocomposite experimental data were not fitted by a simple model of a uniform oxygen diffusion in the bulk. Satisfactory description was obtained only in frames of a more complex model suggesting very fast oxygen exchange between the surface and perovskite–fluorite interfaces in the bulk of composite particles (Fig. 4). This mobile oxygen is exchanged with crystalline domains having a comparable oxygen capacity but different oxygen mobility. Since oxygen self-diffusion coefficients in GDC are known

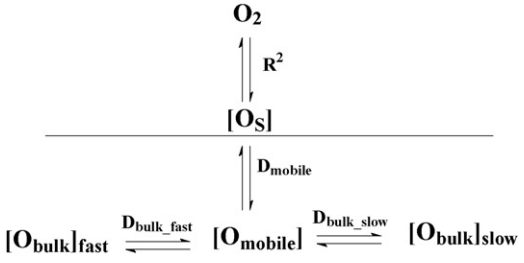

Fig. 4. The heterogeneous model of oxygen isotope exchange on nanocomposite LSNF–GDC. R^2 – the rate of surface exchange, D_{mobile}, D_{fast} and D_{slow} – coefficients of oxygen self-diffusion along interfaces, in the fluorite phase and perovskite phase.

Table 2
The rate of surface oxygen heteroexchange R^2 and coefficients of oxygen self-diffusion in the fluorite phase D_F, perovskite phase D_P and along interfaces $D_{interface}$.

T (°C)	R^2 (molecules/m^{2}s)	D_F (cm^2/s)	D_P (cm^2/s)	$D_{interface}$ (cm^2/s)
600 °C	0.5×10^{19}	$\geq 6 \times 10^{-14}$	2×10^{-14}	$\geq 1 \times 10^{-8}$
700 °C	1.3×10^{19}	$\geq 30 \times 10^{-14}$	9×10^{-14}	$\geq 5 \times 10^{-8}$

to be higher than those in LSCF perovskites possessing the highest oxygen mobility between perovskite-like oxides [1], a faster route of bulk oxygen diffusion was assigned to GDC domains, while a slower one to LSFN domains. Detailed analysis (which is beyond the scope of this paper and will be given elsewhere) revealed that bulk diffusion is the rate-limiting stage only for perovskite domains, while for GDC domains the rate of exchange is controlled by the surface reaction. Hence, for GDC domains only the lowest limits of the oxygen self-diffusion coefficients can be estimated.

Parameters of the surface reaction and bulk diffusion estimated with a due regard for the typical sizes of perovskite and fluorite domains (Table 1) and amount of mobile oxygen atoms located at the perovskite–fluorite interfaces (less than ~2% of the overall oxygen amount in the sample, vide infra) are given in Table 2. Though more detailed analysis is required, the role of perovskite–fluorite interfaces as paths for fast oxygen diffusion in nanocomposites appears to be reliably demonstrated. A fast rate of the surface reaction on nanocomposite is also important for ensuring the efficient activation of oxygen molecules on the air side of membrane. Apparent activation energy of oxygen self-diffusion along perovskite–fluorite interfaces is ~110 kJ/mol, which is close to that in GDC [1].

Oxygen mobility for dense samples. The oxygen chemical diffusion coefficient estimated for dense nanocomposite samples from the weight loss dynamics data following known approaches [30] (Fig. 5) exceeds the values estimated for perovskite. This result also clearly demonstrates a positive role of perovskite–fluorite interfaces as paths for the fast oxygen transfer. The maximum value of the weight loss in these experiments corresponds to removal of less than 2% of the overall amount of oxygen atoms in composite. Apparent activation energy of oxygen chemical diffusion (~110 kJ/mol) coincides with that of the oxygen self-diffusion along perovskite–fluorite interfaces (vide supra). Hence, thus estimated oxygen chemical diffusion coefficient can indeed characterize the oxygen migration along perovskite–fluorite boundary in nanocomposite. The value of the oxygen chemical diffusion coefficient for GDC–$LSFN_{0.3}$ nanocomposite (~10^{-5} cm^2/s at 1080 K) is close to that for the best single-phase MIEC $La_{0.6}Sr_{0.4}Co_{0.8}Fe_{0.2}O_{3-\delta}$ oxide [30].

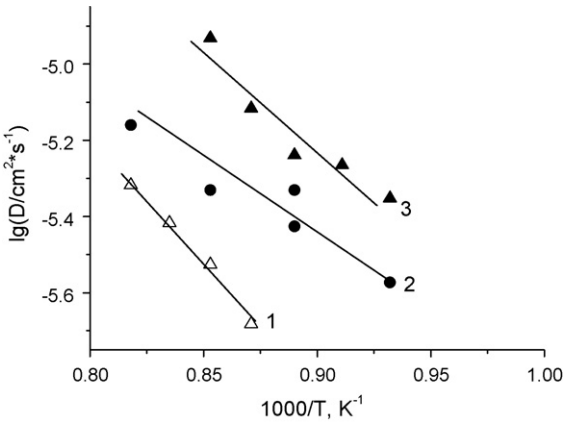

Fig. 5. Temperature dependence of oxygen chemical diffusion coefficient. 1 – $LSFN_{0.3}$, 2 – composite GDC + $LSFN_{0.4}$, 3 – composite GDC + $LSFN_{0.3}$.

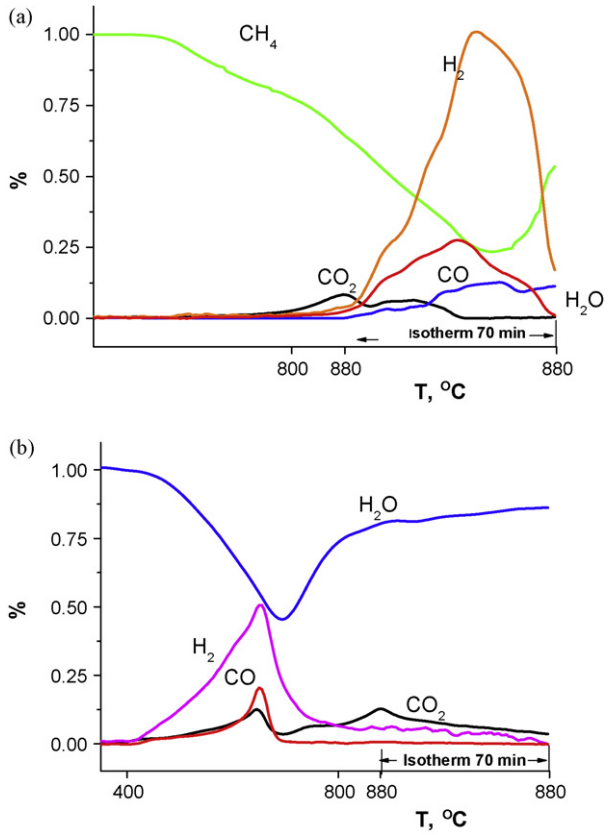

Fig. 6. Typical curves of temperature-programmed reduction by 1% CH_4 in He (a) and subsequent temperature-programmed reoxidation by 1% H_2O in He (b) for MF + GDC nanocomposite calcined at 900 °C under Ar and pretreated under flow of 1% CO_2 in He at 700 °C. Sample weight 0.1 g, flow rate 10 L/h, temperature ramp 5 °/min.

CH_4 TPR/H_2O TPO. For MF + GDC nanocomposite preoxidized in a flow of 1% CO_2 in He after sintering under Ar flow, a high rate of reduction by CH_4 is achieved at high (~900 °C) temperatures (Fig. 6a). However, its reoxidation by H_2O proceeds much faster even at moderate (~700 °C) temperatures. Hence, in reduced state typical for operation of the fuel side of a membrane, this composite could indeed provide a high oxygen flux.

3.2. Testing of a membrane reformer prototype

In all experiments, periodical checking of the exit feed by gas chromatographic analysis on the N_2 admixture revealed its absence within the limit of analysis sensitivity (~0.1%). Hence, membrane retained its integrity and oxygen permselectivity in studied conditions.

As follows from Fig. 7, for feeds with a low CH_4 content, at a low feed rate mainly CH_4 deep oxidation is observed. The increase of the flow of the fuel mixture results in the increase of selectivity of methane conversion into syngas, which is associated with the change of balance between the oxygen flux through the membrane and methane supply. H_2/CO ratio ~2 observed at high flow rates agrees with the stoichiometry of methane partial oxidation into syngas.

Similarly, at a fixed ratio of methane and air flows, the increase of methane concentration in the fuel mixture from 1 to 5 vol.% insignificantly affects the degree of CH_4 conversion, while increasing syngas selectivity (Fig. 8a). However, at a higher concentration of CH_4 in the feed (in the range from 5% to 20%), CH_4 conversion declines strongly at a rather weak variation of SCO and SH_2 (Fig. 8b).

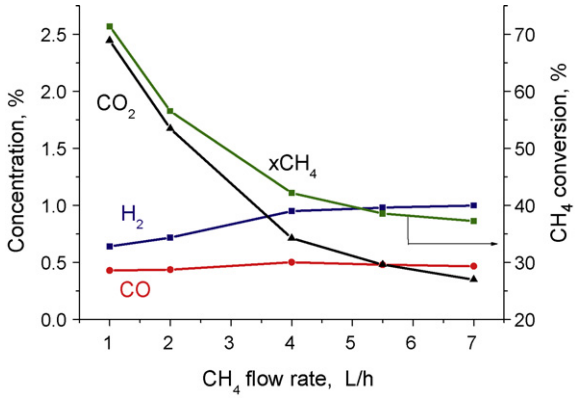

Fig. 7. Dependence of methane conversion, CO and H_2 concentration on the flow rate of 4.5% CH_4 in He at 900 °C. The air flow rate 1.33 L/h.

This means that the oxygen flux is not sufficient to provide a high CH_4 conversion.

In the process of membrane reactor start-up via its heating up to 900 °C in the flow of 4.5% CH_4 in He with the flow rate of 1 L/h followed by its increase up to 5 L/h, both CH_4 conversion and syngas yield were 1.5–2 times higher than stationary values. This suggests that at a low air flow rate nitrogen accumulation in meso–micropores of the membrane occurs, which hampers the oxygen transfer. Indeed, for this rather diluted feed (4.5% CH_4 in He), the increase of the air feed rate has resulted in the increase of the fraction of deep oxidation products due to a higher oxygen flux through the membrane (Fig. 9). However, the situation is reversed for feed with a higher CH_4 content (Fig. 10): CH_4 conversion and syngas concentration in the exit stream increase with the air flow rate.

As expected, at fixed feed and air flow rates, the increase of operation temperature increases CH_4 conversion and syngas yield (Fig. 11). In these experiments, SCO up to 80% and SH_2 up to 60% were obtained. Though higher CH_4 conversions (up to 75%) and CO/H_2 selectivities (up to 80–100%) were observed in diluted feed (Fig. 8), further tuning of operational parameters and membrane porous structure is expected to provide similarly high conversions and syngas yield in concentrated feeds as well. First of all, it concerns the rate of air supply, since the temperature dependence was obtained at air flow rate 3.2 L/h, while increasing the air flow rate up to 20 L/h clearly increased CH_4 conversion (Fig. 10). Estimation of apparent activation energy of the oxygen transfer through the membrane using data of Fig. 11 gives value ~20 kJ/mol, which is much lower than the activation energy of oxygen chemical diffusion in nanocomposite (~110 kJ/mol, vide supra). Hence, at rather low air flow rate, the temperature dependence of the oxygen flux through the membrane and, hence, CH_4 conversion (Fig. 11) appears to be mainly controlled neither by the oxygen transport in the dense layer nor by the surface reactions at the air or fuel side, but by diffusion of oxygen and nitrogen molecules in mesopores and micropores of supported layers known to be characterized by a low activation energy.

For the reaction of CH_4 oxi-dry reforming, the increase of the air flow rate was also accompanied by the increase of CH_4 conversion and syngas content in the converted feed (Fig. 12), apparently caused by the increase of oxygen flux through the membrane. What is even more important is that a higher oxygen flux suppresses formation of C_2H_4 by-product responsible for coking of catalysts.

Hence, these results demonstrate that mass transfer limitations in pores of MIEC layers significantly affect membrane performance. This requires further studies aimed at optimization of the pore structure of substrate and mesoporous/microporous MIEC layers. For a given membrane design, the operation temperature, feed

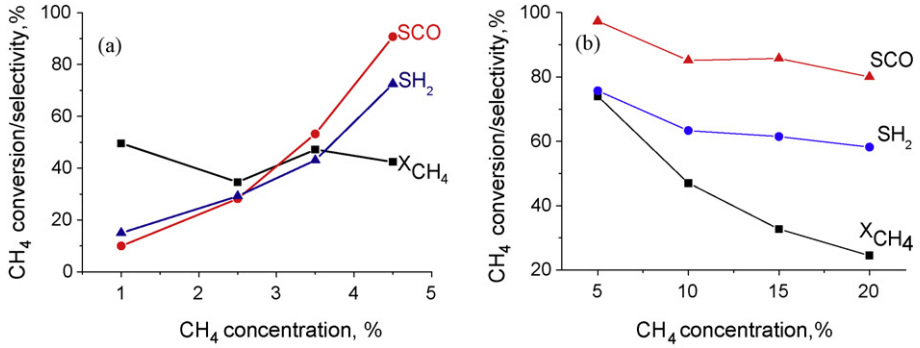

Fig. 8. Dependence of CH_4 conversion, CO and H_2 selectivity on methane concentration in the feed at 900 °C. The fuel flow rate 5 L/h, the air flow rate 1.2 L/h (a) and 2 L/h (b).

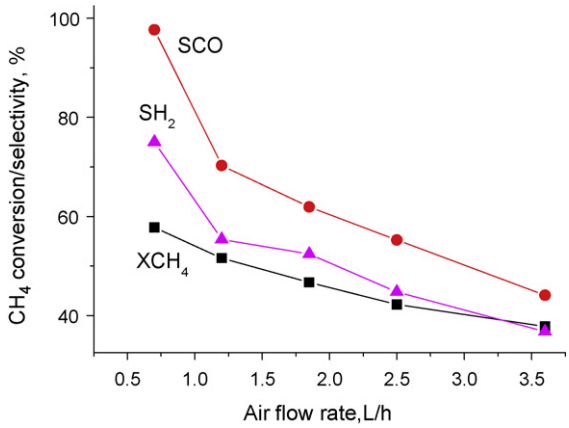

Fig. 9. Effect of the air flow rate on CH_4 conversion, CO and H_2 selectivity at 900 °C. 4.5% CH_4 in He, feed rate 5 L/h.

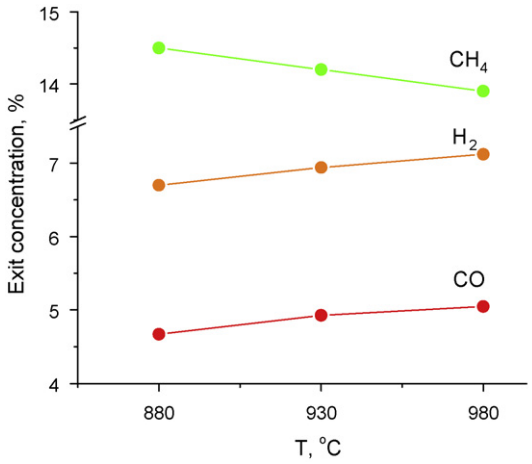

Fig. 11. Effect of temperature on the concentration of components in converted feed. 20% CH_4 in He, feed rate 5 L/h; air flow rate 3.2 L/h.

composition and its flow rate as well as the air flow rate are to be tuned to provide the optimum membrane performance.

Balance estimation revealed that under given conditions the maximum oxygen flux through the membrane is within the limits of 1–2 mLO_2/cm^2 min for 4.5% CH_4 in He and ~5–7 mLO_2/cm^2 min for 20% CH_4 in He, i.e. increases with methane concentration. That is associated with the increase of gradient of oxygen chemical potential across the membrane with the increase of reducing potential of the fuel mixture, which is a driving force for its transfer through the membrane. Therefore, at methane concentration in the input mixture about 50–100% provided a proper tuning of the air flow rate and the porous structure of support and nanocomposite layers, the oxygen flux through membrane is expected to increase at least up to 10–15 mL/cm^2 min, which corresponds to the criterion of membrane suitability for the practical application [2,4].

Testing for at least 100 h at 950–980 °C with feeds containing up to 20% CH_4 demonstrated a stable performance without degradation or coking.

Comparison of achieved level of performance with published data is rather difficult since no data are available in the open literature for performance of metal-supported asymmetric membranes in the reaction of CH_4 partial oxidation into syngas. As far as the

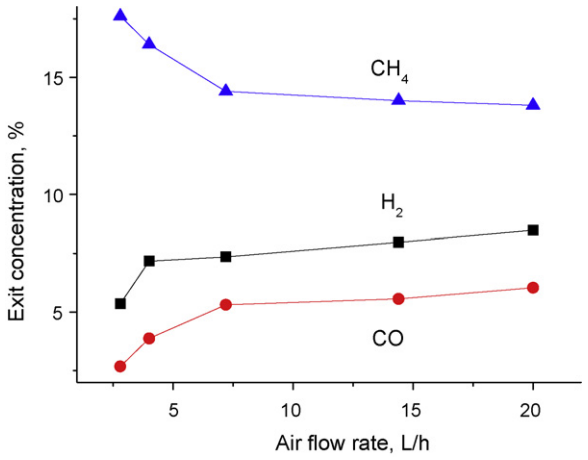

Fig. 10. Effect of the air flow rate on concentration of components in the exit stream at 980 °C. 20% CH_4 in He, feed rate 5 L/h.

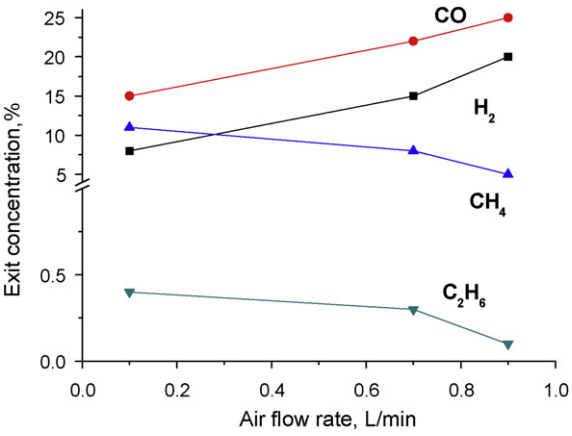

Fig. 12. Effect of air flow rate on the exit stream composition in oxi-dry CH_4 reforming at 930 °C. Feed 20% CO_2 + 20% CH_4 in Ar, feed rate 0.25 L/min.

bulk perovskite membranes are concerned, the highest values of the maximum oxygen flux (up 10 mLO_2/cm^2 min) were reported for Ba–Sr–Co–Fe–O [31–34] or doped $LaGaO_3$ [35,36] perovskites for feeds with CH_4 content up to 80% with loaded layers of different Ni-containing granulated catalysts of CH_4 reforming These values are comparable with results obtained in our work (vide supra). Lower values of oxygen flux (0.5–4 mLO_2/cm^2 min) were obtained for membranes comprised of SDC-covered LaSrCoFeO 6482 disc [23] or layered $La_2Ni_{0.9}Co_{0.1}O_{4+\delta}$ perovskites [37]. Hence, designed membrane even though not optimized is comparable with the best samples by oxygen permeability.

Comparison of CH_4 conversion and syngas yields is also quite demanding task due to variety of flow rates, configuration of reactors and catalytic layers etc, which makes difficult reliable estimation of contact times required for meaningful comparison of performance. A lot depends also on the heat balance within reactors especially when they operate in the mode of complete methane combustion on the membrane surface followed by subsequent steam and dry reforming [37]. However, the maximum levels of CH_4 conversion and syngas selectivity (up to 70–80%) obtained in this work (vide supra) are at least comparable with the best reported results for Ba–Sr–Co–Fe–O perovskites [31–34]. At the same time, for other membrane systems, lower values of CH_4 conversion (5–40%) [14,35–37] and syngas selectivity (5–17%) [37] were reported.

To increase methane conversion and syngas yield at its high inlet concentration, first of all, the process parameters are to be tuned, namely, the air flow rate and contact time are to be increased. If acceptable from the point of view of syngas composition for the final application, CO_2 or H_2O can be added into the feed, which indeed helps to increase conversion (Fig. 12). Second, as clear follows from the results of this research, the porous structure of Ni–Al substrate and mesoporous/microporous MIEC layers is to be optimized to overcome diffusion limitations from the air side. Thus, functionally graded design of Ni–Al foam substrate is to be applied consisting of highly porous (~80% porosity) main part with a thickness ~1–2 mm (provides required mechanical strength of membrane) covered by a thin (<0.1 mm) compressed Ni–Al foam layer with porosity ~40–50% (serves as support for nanocomposite oxygen-permeable layers). Similarly, the thickness of mesoporous and microporous mixed ionic–electronic conducting layers is to be further decreased while their pore size is to be increased, eliminating, if possible, the microporous layer at all. Next, preparation procedures are to be modified providing covering of the walls of mesopores by perovskite LSFN nanoparticles highly efficient in activation of oxygen molecules, thus enhancing the surface oxygen diffusion flux within mesopores towards the dense permselective layer. At last, the pore structure and composition of the catalytic layer covering the dense membrane layer can be further optimized with a due regard for improving its transport properties (to avoid any diffusion limitations for CH_4 molecules) while providing high concentration of surface sites for CH_4 activation and a good contact with the surface of dense permselective layer to ensure fast transfer of oxygen atoms from the membrane onto the surface of catalyst particles."

4. Conclusion

LSFN–GDC nanocomposites prepared via ultrasonic dispersion of powders in organic solvents with addition of surfactants demonstrate a high oxygen mobility due to a positive role of perovskite–fluorite interfaces as paths for fast oxygen migration.

Procedures for design of asymmetric oxygen-conducting membranes comprised of MIEC layers with graded porosity and composition (LSNF–GDC and MF–GDC) supported on compressed foam Ni–Al planar substrate were elaborated.

Testing of methane reformer prototype equipped with these membranes demonstrated a good and stable performance promising for the up-scaling and practical application.

Acknowledgements

This work is supported by Project 57 of RAS Presidium Program No. 27, RFBR-ofi_m 09-03-12317, ISTC 3234 and OCMOL FP7 Projects, and Contract 02.740.11.0852 of the Federal Program "Scientific and Educational Cadres of Russia".

References

[1] A. Esquirol, J. Kilner, N. Brandon, Solid State Ionics 175 (2004) 63.
[2] A.V. Kovalevsky, V.V. Kharton, F.M.M. Snijkers, J.F.C. Cooymans, J.J. Luyten, J.R. Frade, Solid State Ionics 179 (2008) 61.
[3] X. Zhu, W. Yang, AIChE J. 54 (2008) 665.
[4] B.A. van Hassel, Solid State Ionics 174 (2004) 253.
[5] H.J.M. Bouwmeester, H. Kruidhof, A.J. Burggraaf, Solid State Ionics 72 (1994) 185.
[6] K. Watanabe, M. Yuasa, T. Kida, K. Shimanoe, Y. Teraoka, N. Yamazoe, Chem. Mater. 20 (2008) 6965.
[7] H. Takamura, T. Kobayashi, T. Kasahara, A. Kamegawa, M. Okada, J. Alloys Compd. 408–412 (2006) 1084.
[8] A. Thursfield, I.S. Metcalfe, J. Mater. Chem. 14 (2004) 2475.
[9] H.J.M. Bouwmeester, Catal. Today 82 (2003) 141.
[10] A. Juble, D. Farrusseng, C. Guizard, Catal. Today 104 (2005) 102.
[11] X. Dong, Z. Liu, W. Jin, N. Xu, J. Power Sources 185 (2008) 1340.
[12] H. Takamura, M. Ogawa, K. Suehiro, H. Takahashi, M. Okada, Solid State Ionics 179 (2008) 1354.
[13] H. Kusaba, Y. Shibata, K. Sasaki, Y. Teraoka, Solid State Ionics 177 (2006) 2249.
[14] Sh. Miyoshi, T. Furuno, H. Matsumoto, T. Ishihara, Solid State Ionics 177 (2006) 2269.
[15] V.V. Zyryanov, V.A. Sadykov, G.M. Alikina, Sep. Sci. Technol. 42 (2007) 2849.
[16] K. Watanabe, M. Yuasa, T. Kida, K. Shimano, Y. Teraoka, N. Yamazoe, Solid State Ionics 179 (2008) 1377.
[17] A. Leonov, A. Romashko, in: J. Banhart, N. Fleck (Eds.), Cellular Metals: Manufacture, Properties, Applications. Intern. Conf. on Cellular Metal Foaming Technology "*MetFoam 2003*", Verl. MIT Publ., Berlin, 2003, p. 275.
[18] O. Smorygo, V. Mikutski, A. Marukovich, Yu. Vialiuha, A. Ilyushchanka, N. Mezentseva, G. Alikina, Z. Vostrikov, Yu. Fedorova, V. Pelipenko, R. Bunina, V. Sadykov, Int. J. Hydrogen Energy 34 (2009) 9505.
[19] V. Sadykov, V. Sobyanin, N. Mezentseva, G. Alikina, Z. Vostrikov, Yu. Fedorova, V. Pelipenko, V. Usoltsev, S. Tikhov, A. Salanov, L. Bobrova, S. Beloshapkin, J.R.H. Ross, O. Smorygo, V. Ulyanitskii, V. Rudnev, Fuel 89 (2010) 1230.
[20] V. Sadykov, S. Pavlova, V. Zarubina, A. Bobin, G. Alikina, A. Lukashevich, V. Muzykantov, V. Usoltsev, T. Kharlamova, A. Boronin, S. Koscheev, T. Krieger, A. Ishchenko, N. Mezentseva, A. Salanov, A. Smirnova, O. Bobrenok, N. Uvarov, ECS Trans. 25 (2009) 2403.
[21] V. Sadykov, T. Kharlamova, L. Batuev, V. Muzykantov, N. Mezentseva, T. Krieger, G. Alikina, A. Lukashevich, V. Rogov, V. Zaikovskii, A. Ishchenko, A. Salanov, A. Boronin, S. Koscheev, S. Pavlova, N. Uvarov, A. Smirnova, O. Vasylyev, Compos. Interfaces 16 (2009) 407.
[22] V. Sadykov, T. Kharlamova, L. Batuev, N. Mezentseva, G. Alikina, V. Muzykantov, T. Krieger, S. Pavlova, V. Zaikovskii, A. Ishchenko, V. Zarubina, V. Rogov, O. Bobrenok, N. Uvarov, J. Kilner, J. Druce, A. Smirnova, Mater. Res. Soc. Symp. Proc. 1098 (2008) 1–6, 1098-HH07-06.
[23] E.D. Wachsman, T.L. Clites, J. Electrochem. Soc. 149 (3) (2002) A424.
[24] U. Balachandran, J.T. Dusek, R.L. Mieville, R.B. Poeppel, M.S. Kleefisch, S. Pei, T.P. Kobylinski, C.A. Udovich, A.C. Bose, Appl. Catal. A: Gen. 133 (1995) 19.
[25] E.M. Sadovskaya, Yu.A. Ivanova, L.G. Pinaeva, G. Grasso, T.G. Kuznetsova, A. van Veen, V.A. Sadykov, C. Mirodatos, J. Phys. Chem. A 111 (2007) 4498.
[26] V. Sadykov, V. Muzykantov, A. Bobin, N. Mezentseva, G. Alikina, N. Sazonova, E. Sadovskaya, L. Gubanova, A. Lukashevich, C. Mirodatos, Catal. Today (2010), doi:10.1016/j.cattod.2010.03.064.
[27] Yu.V. Ulyanitskii, A.A. Shterzer, S.B. Zlobin, V.I. Matrenin, I.V. Schipanov, Yu.S. Serykh, A.S. Stikhin, L.M. Tretyakova, V.A. Sadykov, S.N. Pavlova, S.F. Tikhov, V.A. Kuzmin, Altern. Energ. Ecol. 9 (2006) 137.
[28] Sh. Wang, T. Kato, S. Nagata, T. Honda, T. Kaneko, N. Iwashita, M. Dokiya, Solid State Ionics 146 (2002) 203.
[29] V.A. Sadykov, Yu.V. Borchert, G.M. Alikina, A.I. Lukashevich, N.V. Mezentseva, V.S. Muzykantov, E.M. Moroz, V.A. Rogov, V.I. Zaikovskii, D.A. Zyuzin, N.F. Uvarov, A.V. Ishchenko, V.V. Zyryanov, A. Smirnova, Glass Phys. Chem. 33 (2007) 320.
[30] M. Katsuki, Sh. Wang, M. Dokiya, T. Hashimoto, Solid State Ionics 156 (2003) 453.
[31] Z. Shao, H. Dong, G. Xiong, Y. Cong, W. Yang, J. Membr. Sci. 183 (2001) 181.
[32] H. Wang, Y. Cong, W. Yang, Catal. Today 82 (2003) 157.

[33] Z. Shao, G. Xiong, H. Dong, W. Yang, L. Lin, Sep. Purif. Technol. 25 (2001) 97.
[34] H. Dong, Z. Shao, G. Xiong, J. Tong, S. Sheng, W. Yang, Catal. Today 67 (2001) 3.
[35] T. Ishihara, Y. Tsuruta, T. Todaka, H. Nishiguchi, Y. Takita, Solid State Ionics 152 (2002) 709.
[36] T. Ishihara, T. Yamada, H. Arikawa, H. Nishiguchi, Y. Takita, Solid State Ionics 135 (2000) 631.
[37] V.V. Kharton, A.A. Yaremchenko, E.V. Tsipis, A.A. Valente, M.V. Patrakeev, A.L. Shaula, J.R. Frade, J. Rocha, Appl. Catal. A: Gen. 261 (2004) 25.